Confinement Effect of Mesopores: In Situ Synthesis of Cationic Tungsten-Vacancies for a Highly Ordered Mesoporous Tungsten Phosphide Electrocatalyst

Feng Li, Chengru Wang, Xiaocang Han, Xiaoqian Feng, Yuqi Qu, Jing Liu,* Wenlong Chen, Liping Zhao, Xuefeng Song, Hong Zhu, Han Chen, Min Zhao, Zhao Deng, Jianbo Wu, Peng Zhang,* and Lian Gao

ACCESS | Metrics & More | Article Recommendations | Supporting Information

ABSTRACT: Engineering defects in crystalline electrocatalysts is an effective approach to tailor the electronic structure and number of active sites, which are essential for the intrinsic activity of the hydrogen evolution reaction (HER). Unlike previously reported methods, we demonstrate a confinement effect using a mesoporous template for in situ fabrication of cationic W vacancies in as-prepared ordered mesoporous tungsten phosphide (WP) nanostructures by adjusting the nonstoichiometric ratio of the precursor elements. With a plenty of W vacancies and ordered mesoporosity, the as-prepared catalyst WP-Mesop exhibits better catalytic performance than the catalysts without mesopores and/or vacancies. The WP-Mesop shows an ultralow overpotential of 175 mV in acid and 229 mV in alkaline at 100 mA cm^{-2} and stability of 48 h without structural collapse in both acid and alkaline media. Meanwhile, density functional theory calculations further reveal that the activation barrier for HER can be lowered by introducing cationic W vacancies. This strategy can be extended to generate cationic defects in other transition metal phosphides to improve their HER activities.

KEYWORDS: tungsten phosphide, ordered mesoporous, confinement effect, cation vacancies, DFT calculations
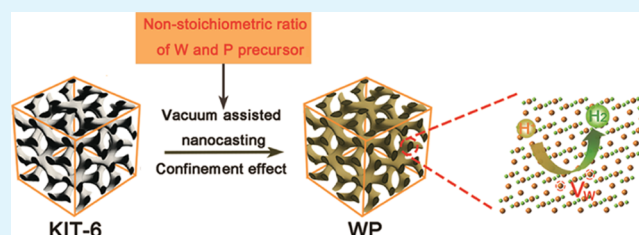
1. INTRODUCTION

Electrochemical water splitting represents one of the most important solutions for mass-producing hydrogen.[1−3] Noble metals, for example, Pt and Pd, possess exceptional activity with nearly zero overpotential in acid media.[4] However, the development of nonprecious electrocatalysts is more attractive because of their costs and natural abundance. It is a critical challenge to identify alternative earth-abundant catalysts for their widespread use.

Transition metal compounds such as carbides,[5−7] nitrides,[8,9] sulfides,[10−13] selenides,[14] and phosphides[15−18] have shown catalytic activity in the hydrogen evolution reaction (HER) (see comparison in Figure S1). Among them, transition metal phosphides (TMPs) also show potential applications in HER in both acid and alkaline media. Up to now, Fe, Co, Ni, Cu, Mo, and W have been used to make phosphide catalysts for electrochemical hydrogen evolution.[19] Many efforts have also been devoted to designing TMPs catalysts with enhanced HER activity.[20−27] Electronic structures and morphology engineering are the most effective strategies to develop new generations of electrocatalysts.

Different from perfect crystals, defective sites usually present unique electronic properties that exert a positive impact on reactivity.[28,29] Point defects, or vacancies, have emerged as a potential way to alter the electronic structure of solid electrocatalysts. Many experimental methods have been developed to fabricate vacancies in crystalline materials. Postfunctionalized methods such as ball milling, plasma etching, and steam etching are well established for metals, metal oxides, carbons, and transition-metal dichalcogenides.[30−34] However, these methods suffer from poor controllability, inhomogeneity, or structural collapse. As compared to post-treating methods, in situ synthesis is a more promising and attractive way to fabricate vacancies.[35] Chemical leaching of substitutional dopants is regarded as a feasible in situ approach such as doping of Mg in FeP to form Fe vacancies.[36] However, difficulties still remain in the selection of suitable sacrificial dopants for their widespread use. New facile and controllable methods of vacancy engineering must be developed.

In addition to optimization of electronic structures, morphology engineering is regarded as a practical strategy to improve HER activity as catalysis takes place on the surface. Precise control over the catalyst surface structure with suitable morphologies may provide more active sites and facilitate mass diffusion pathways for HER. Extensive exploration has been devoted to developing specific architectures such as nanowires, nanorods, nanosheets, and so on.[37]

Recently, porous materials with abundant and controlled pore sizes are of particular interest in electrocatalysis. For instance, Sun et al. reported three-dimensional macroporous multishelled Ni_2P microspheres with specific surface area of 31.6 m^2/g as an active catalyst for hydrogen evolution.[38] This unique morphology could provide more and accessible active sites, facilitating the HER process. Hu and co-workers developed hierarchical Ni−Co−P hollow nanobricks electrocatalysts, which exhibited a low overpotential of 107 mV to drive a current density of 10 mA cm^{-2} for HER.[39] Ordered mesoporous materials have larger specific surface area than their macroporous forms. In addition, mesopores are better than micropores for electrolyte diffusion. Therefore, it is believed that TMPs with ordered mesopores could perform well in HER catalysis. However, there are few reports available regarding ordered mesoporous TMPs.

Herein, we explore a confinement effect of the mesoporous template to in situ synthesize both cationic W vacancies and mesoporous structures in tungsten phosphide (WP). To the best of our knowledge, this seems to be the first successful preparation of highly ordered mesoporous WP. We report here the synthesis of ordered mesoporous WP with abundant W vacancies (∼10%), which was successfully prepared using nonstoichiometric ratios of W and P (P/W = 1.1). The formation mechanism of this unique structure was investigated. The as-prepared mesoporous WP exhibited enhanced activity and stability toward the HER, as compared to nonmesoporous WP nanoparticles in both acid and alkaline solutions, showing an ultralow overpotential of 175 mV in acid and 229 mV in alkaline at 100 mA cm^{-2} and stability of 48 h for HER. Our work proves that a combination of mesoporosity and high density defects provides good opportunities to tailor electrocatalytic properties.

2. EXPERIMENTAL SECTION

2.1. Synthesis of Mesoporous, Nanostructured, and Bulk WP Powders.
Mesoporous WP was synthesized by nanocasting using a cubic $Ia\overline{3}d$ mesoporous silica template KIT-6. The KIT-6 template with a Brunauer−Emmett−Teller (BET) specific surface area of ∼770 m^2/g and an average pore size of ∼8 nm was prepared, according to previously reported procedures.[40] In a typical vacuum-assisted nanocasting process, 0.35 mmol of phosphotungstic acid ($H_3O_{40}PW_{12}·xH_2O$, Alfa Aesar) and 493 mg of phosphoric acid (H_3PO_4, 85 wt %, Sinopharm) were added into 6 mL of absolute ethanol (99.8%, Sinopharm) to form a homogeneous precursor solution. The atomic ratio of P/W in the precursor was 1.1. Then, the precursor solution was mixed with 500 mg of mesoporous silica KIT-6 in a glass tube (20 cm long) and stirred for 1 h. After that, the air in the glass tube and pores was evacuated for 4 h. Thereafter, the precursor solution was successfully introduced. A further overnight drying at 50 °C under vacuum was carried out to obtain dry powders. The powders were then calcined at 300 °C for 4 h in air. After that, the precursor powders were placed into a quartz boat and then reduced in a tube furnace (OTF-1500X, MTI Corporation) at 700 °C for 16 h in a H_2/Ar atmosphere (20% H_2) at a heating rate of 2 °C min^{-1}. The calcined sample was treated in 2 M KOH aqueous solution at 50 °C for 8 h to remove the silica template, followed by

washing with Milli-Q water three times and freeze-drying under vacuum. The obtained sample was denoted as WP-Mesop. Another control sample was prepared using the same nanocasting method as mentioned above with P/W = 1.0 and labeled as WP-Mesop-A. For comparison, WP nanoparticles (WP-Nano) were obtained following the same procedure in the absence of KIT-6 template. The samples with different atomic proportions of P in the precursor solution were also prepared, denoted as WP-Nano-2 (P/W = 2) and WP-Nano-4 (P/W = 4). A bulk WP (WP-Bulk) was prepared by replacing the phosphorous precursor with diammonium phosphate $[(NH_4)_2·HPO_4]$.

2.2. Physical Characterizations.
The as-prepared samples were characterized by X-ray diffraction (XRD, Rigaku D/max 2550) with Cu Kα radiation. Small-angle X-ray scattering (SAXS) patterns were recorded by a SAXSess mc^2 with Cu Kα radiation for mesoporous WP samples. Nitrogen adsorption−desorption isotherms were performed on an automated gas sorption analyzer (Autosorb iQ, Quantachrome Instruments). Low-resolution transmission electron microscopy (TEM) images were obtained from FEI Tecnai G2 (120 kV). Scanning TEM (STEM), Cs-corrected STEM, high-angle annular dark-field STEM (HAADF-STEM), and energy dispersive X-ray (EDX) mapping profiles were acquired by a FEI Titan Themis Cubed G2 30−300 microscope operated at 300 kV. X-ray photoelectron spectroscopy (XPS) was conducted using a Kratos AXIS Ultra DLD spectrometer with monochromatic Al Kα source (1486.6 eV) to identify the surface chemical states. The XPS spectra of W 4f were fitted into peak doublets with parameters of spin−orbit separation $\Delta E(4f_{5/2}-4f_{7/2}) = 2.1 \pm 0.1$ eV and intensity ratio $4f_{5/2}/4f_{7/2} = 0.75$. The fitted of P 2p were confined to $\Delta E(2p_{1/2}-2p_{3/2}) = 0.9 \pm 0.1$ eV and intensity ratio $2p_{1/2}/2p_{3/2} = 0.5$.

2.3. Electrochemical Measurements.
The as-prepared catalysts were loaded onto a glassy carbon (GC) working electrode. Typically, 10 mg of catalyst and 20 μL of Nafion solution (5 wt %, DuPont Corporation) were mixed with 980 μL of water−ethanol solution (volume ratio: 1:1). The suspension was sonicated for 30 min to form a homogeneous ink. Then, 14 μL of the ink was dripped onto a 3 mm diameter GC and dried at room temperature overnight. The mass loading was ∼2 mg cm^{-2}. Electrochemical measurements were performed in 0.5 M H_2SO_4 and 1 M KOH solutions using an electrochemical workstation (Biologic VMP3) with a three-electrode system. A 5 mm diameter graphite rod (99.997%, Alfa Aesar) was used as the counter electrode in both acid and alkaline solution. An Ag/AgCl electrode and a Hg/HgO electrode served as reference electrodes in 0.5 M H_2SO_4 and 1 M KOH electrolyte, respectively. The Ag/AgCl and Hg/HgO reference electrodes were calibrated to reversible hydrogen electrode (RHE) in H_2 saturated 0.5 M H_2SO_4 and 1 M KOH electrolyte, respectively, using platinum for both working and counter electrodes. The calibration results (Figure S11) show the equations of $E(RHE) = E(Ag/AgCl) + 0.229$ V and $E(RHE) = E(Hg/HgO) + 0.909$ V. Linear sweep voltammetry (LSV) measurements were performed at a sweep rate of 2 mV s^{-1} at room temperature. The onset potential here is defined as the overpotential to drive the HER with a current density of 1 mA cm^{-2}. The electrochemical impedance spectroscopy (EIS) was performed from 120 kHz to 0.1 Hz at a potential of −100 mV versus RHE with a sinusoidal voltage of 5 mV. The stability test was carried out under the electrochemical mode of constant current at a current density of 10 mA cm^{-2} for 48 h.

2.4. Computational Details and Models.
Density functional theory (DFT) calculations with van der Waals correction of DFT-D2 method were performed by using the Vienna Ab initio Simulation Package.[41,42] The interaction between core and valence electrons was described by the projector augmented wave, and generalized gradient approximation with the Perdew−Burke−Ernzerhof exchange correlation functional was used within the calculations.[43] During the geometric optimization, 500 eV energy cutoff for plane-wave basis was set, while the convergence criteria for electronic and ionic relaxation were 10^{-4} eV and 0.02 eV/Å, respectively. Γ-centered k-points of 5 × 10 × 5 was performed in bulk WP optimization, and 5 × 5 × 1 Γ-centered k-points with dipolar correction was included in the slab WP
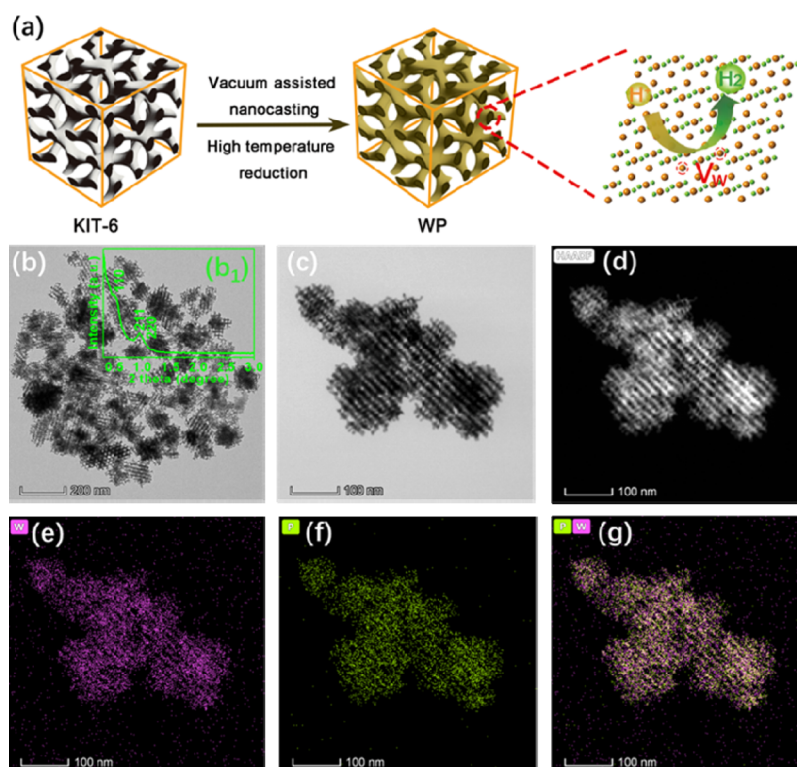
Figure 1. (a) Synthesis of mesoporous WP with plenty of W vacancies for HER. (b,c) Low-resolution TEM images and the inset (b$_1$) is SAXS profile. (d) HAADF-STEM image. (e–g) Corresponding STEM−EDX elemental mappings of WP-Mesop.

model optimization. For WP slab model, $1 \times 2 \times 1$ slab supercell including six atomic layers was separated by a 15 Å thick vacuum layer. During the calculation, the upper two layers were fully relaxed, and the remaining four-layer atoms were fixed. We investigated the catalytic activity for HER on the most exposed (101) surface, whose surface energy was evaluated as $\gamma = 2.690$ J/m^2 in our computation. The adsorption free energy (ΔG_{H*}) of the hydrogen atom, which can be used to reliably indicate the catalytic activity of the site toward HER, can be estimated by following equations[44]

$$\Delta E = E(\text{slab} + \text{H}) - E(\text{slab}) - 1/2 E(\text{H}_2)$$

$$\Delta G_{H*} = \Delta E + \Delta ZPE - T\Delta S$$

where the $E(\text{slab} + \text{H})$ and $E(\text{slab})$ are the total energy of slab with one hydrogen atom on the (101) surface and the total energy of slab without any hydrogen atom, respectively. $E(\text{H}_2)$ is the total energy of a gas hydrogen molecule. Therefore, the ΔE is the absorption energy of the hydrogen atom on the 1×2 WP(101) surface. ΔZPE and ΔS are the zero-point vibrational energy and entropy change, respectively.

3. RESULTS AND DISCUSSION

Synthesis of ordered mesoporous WP by nanocasting is shown schematically in Figure 1a. The ordered mesoporous structure of KIT-6 was confirmed by TEM, SAXS profile, and N$_2$ adsorption−desorption isotherm, as shown in Figures S2−S4. The mesoporous structures of the obtained WP labeled as WP-Mesop after silica removal were characterized by TEM, SAXS, and isothermal adsorption−desorption curve. Figure 1b,c shows low-resolution TEM images of the obtained WP-Mesop, which reveal that WP-Mesop possesses a highly ordered mesoporous structure. Almost all the observed WP particles are mesoporous with average pore sizes of ~8 nm (Figure S5). The SAXS pattern of WP-Mesop, as shown in the inset of Figure 1b, can be assigned to $Ia(\overline{3})d$, giving the same scattering pattern as the original KIT-6 templates, as shown in

Figure S3. This further confirms the highly ordered mesoporous structure of the obtained WP. The N$_2$ adsorption−desorption isotherms (Figure S6) show an obvious hysteresis loop for WP-Mesop, suggesting that the results are consistent with TEM and SAXS. The BET-specific surface area of WP-Mesop measured from N$_2$ adsorption is ~37 m^2/g, which is almost the same as WP-Mesop-A (~36 m^2/g, Figure S7) and is twice that of WP-Nano (~18 m^2/g), as listed in Table S1. Local elemental distribution of the WP-Mesop sample was carried out using an EDX spectrometer in the STEM mode. The EDX mappings were acquired with an HAADF-STEM image, as shown in Figure 1d−g. The chemical mappings reveal that W and P atoms are homogeneously distributed throughout the WP-Mesop structure.

Figure 2a shows a typical Cs-corrected high-resolution STEM (HR-STEM) image of WP-Mesop viewed along the [221] zone axis. It can be seen that many darker spots, marked by red arrows, are randomly distributed among the bright ones in the nanocrystal. The zoom-in and colored image (Figure 2b) selected from Figure 2a emphasizes the intensity difference and dark contrast. As compared to the well-established simulated HR-STEM image (Figure 2c) of a perfect crystal, sites with dark contrast correspond to the point defects.[45] It should be noted that these point defects would be attributed to the presence of rich P vacancies or W vacancies. The existence of defects is also revealed by the XRD profiles. As shown in Figure 2d,d$_1$, all the diffraction peaks of WP-Mesop shift significantly (~0.3° for 2θ) to larger angles, as compared to WP-Nano, indicating a decrease in the lattice spacing. This lattice contraction may be caused by the introduction of the ionic vacancies. On the basis of the EDX results (Table S2), the point defects should be attributed to W vacancies because the W/P stoichiometric ratio of the sample is 90/100,
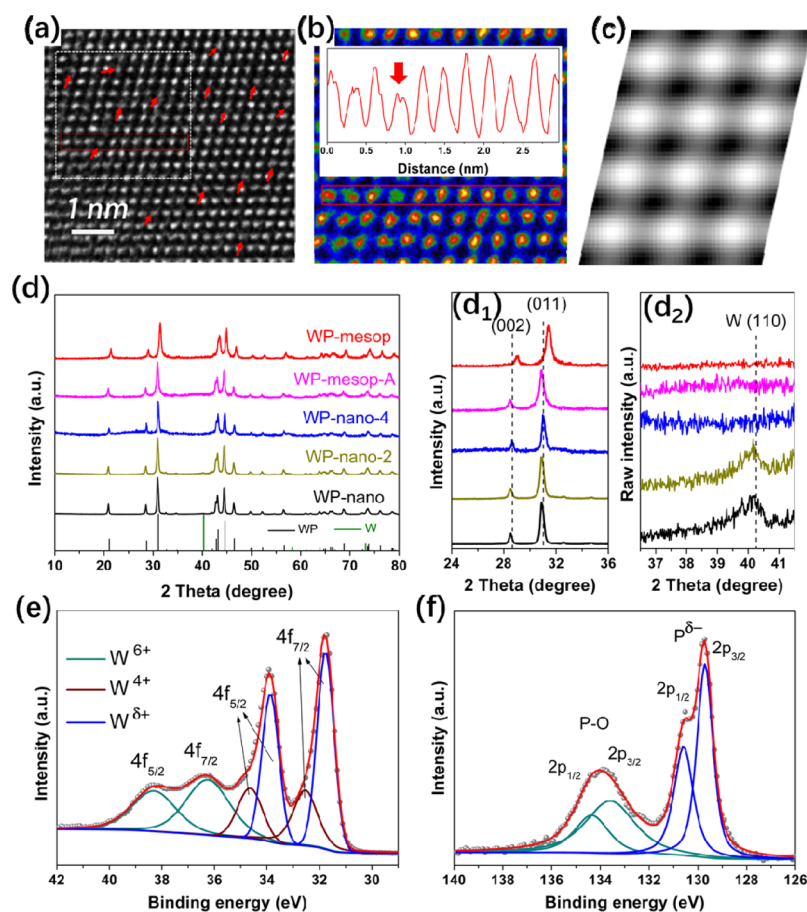
Figure 2. (a) High-resolution Cs-corrected STEM image of WP-Mesop with the [221] zone axis. (b) Colored HR-STEM image with a profile plot of a line of atoms. (c) Simulated HR-STEM image of WP oriented along the [221] axis using MacTempasX-2 software. (d) XRD patterns of WP-Mesop, WP-Mesop-A, WP-Nano, WP-Nano-2, and WP-Nano-4. (d_1,d_2) are the enlarge selected areas of XRD. (e,f) XPS spectra of WP-Mesop around the BE of W 4f and P 2p.

indicating a deficiency of W atoms by ∼10%. XPS results further confirm the presence of W vacancies in the WP-Mesop (Table S2). The surface W/P of the WP-Mesop is ∼71%, which deviates from the theoretical stoichiometric proportion. The details of the XPS results are discussed below.

It is worth pointing out that the as-prepared WP-Nano possesses a small extra diffraction peak at around 40° (Figure 2d_2), which can be assigned to the (110) diffraction of metallic tungsten (PDF no. 89-4900). Interestingly, when we increased the atomic proportion of P in the precursor solution to P/W = 2 for the preparation of WP-Nano-2, metallic W still forms after reduction. Phase pure WP (WP-Nano-4) was obtained when the P/W ratio was increased to 4. This indicates that the precursor loses P during reduction. In the limited domain of the mesoporous template (WP-Mesop and WP-Mesop-A), however, no impurity diffraction peaks can be observed in the XRD (Figure 2d_2), suggesting obvious restraint of P loss.

Generally, high temperature reduction of P precursor might result in formation of volatile P_4, reducing the P content in WP. However, motion of atoms is restrained in the limited domain of the mesopores, hence the P is likely constrained inside the pores and facilitates formation of WP crystals at 700 °C rather than evaporating. For WP-Mesop-A, phase pure WP can be obtained because the P/W ratio in the precursor is 1.0. When the P/W ratio increases to 1.1, the P-rich precursor tends to form W vacancies in WP. Therefore, there are two key factors for defective WP formation, one is a proper

nonstoichiometric ratio of the precursor (P/W > 1). The other is reduction in the limited domain of the mesoporous template to prevent P loss. This strategy has not been reported earlier. Similar defect-rich materials are usually synthesized using structure reconstruction or confinement effect of inhomogeneous precursor area such as W_xC and Mo_xC.[46,47]

The mesoporous WP sample with P/W = 2 in the precursor was also explored. However, its mesoporous structure is not as ordered as the former one (Figure S9). This can be ascribed to the excess P_4 formation and/or deficient W in the pores, which leads to discontinuous WP crystals in the constrained porous channels.

The nature of the catalyst surface is essential to HER performance. XPS was used to determine the chemical states of the WP-Mesop surface. The XPS, as shown in Figure 2e,f, confirms the existence of W and P in the WP-Mesop sample. The high-resolution XPS spectrum of W_{4f} (Figure 2e) can be divided into three sets of W species. A pair of major peaks with lower binding energy (BE) located at approximately 31.8 and 33.9 eV can be assigned to W $4f_{7/2}$ and W $4f_{5/2}$ of $W^{\delta+}$ (0 < δ < 4) bonded with P atoms, respectively. In addition to the two predominant peaks, two other sets of relatively weak peaks appear at 32.5, 34.6, 36.2, and 38.3 eV and can be attributed to W^{4+} and W^{6+} because of the trace amounts of tungsten oxides. In the P 2p region (Figure 2f), the predominant P species at 129.7 and 130.6 eV correspond to $2p_{3/2}$ and $2p_{1/2}$, respectively and can be indexed to $P^{\delta-}$ bonded to W atoms. The oxidation
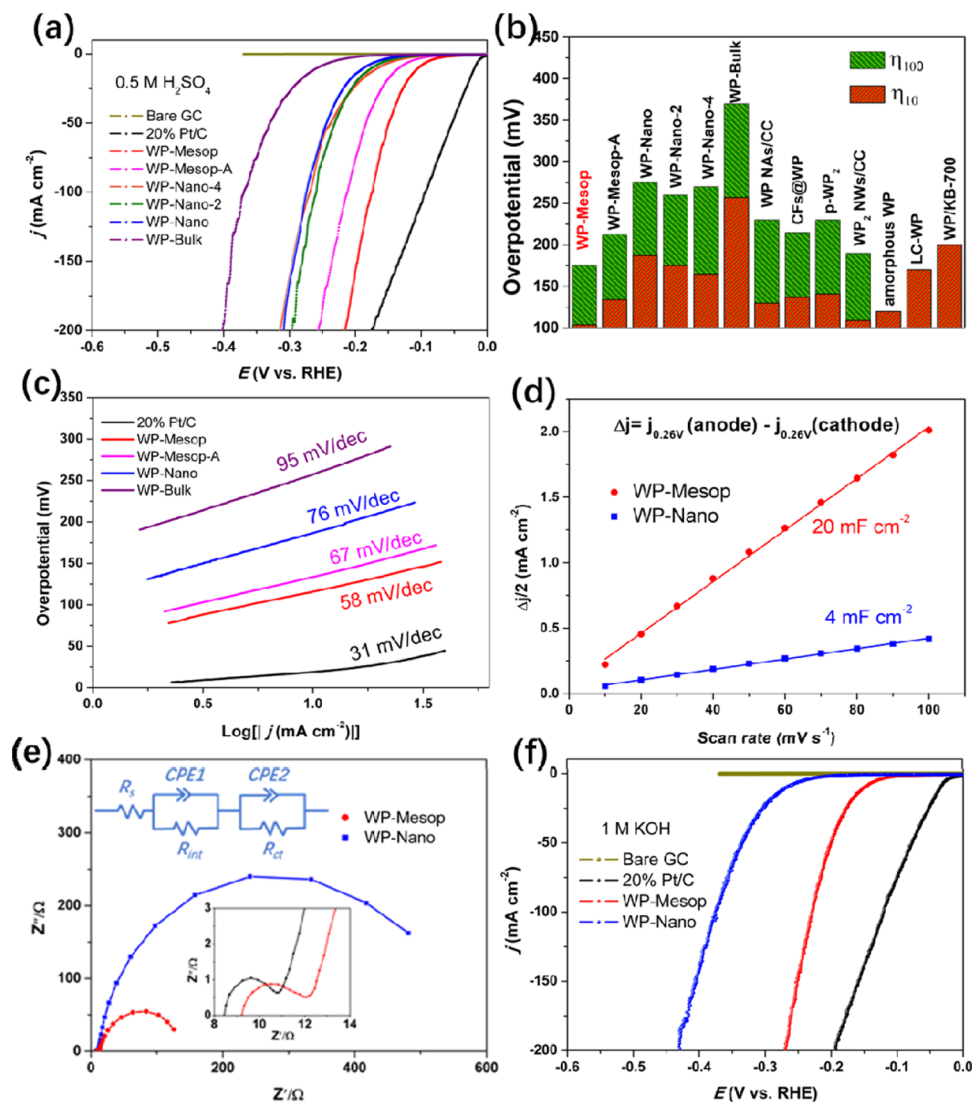
Figure 3. (a) LSV curves of bare GC, Pt/C, WP-Mesop, WP-Mesop-A, WP-Nano, WP-Nano-2, WP-Nano-4, and WP-Bulk in 0.5 M H_2SO_4 solution. (b) HER overpotential of η_{10} and η_{100} for each catalyst. (c) Corresponding Tafel slopes acquired from the linear section of LSV. (d) Measured capacitive currents at 0.26 V vs RHE as a function of the scan rate for WP-Mesop and WP-Nano in 0.5 M H_2SO_4. (e) Nyquist plots for WP-Mesop and WP-Nano at a potential of −100 mV vs RHE in 0.5 M H_2SO_4. (f) LSV curves of bare GC, Pt/C, WP-Mesop, and WP-Nano in 1 M KOH aqueous electrolyte.

Table 1. Summary of the Catalytic Performance of Each WP Catalyst

sample	electrolyte	onset potential (mV)	η_{10} (mV)	η_{100} (mV)	Tafel slop (mV/dec)	j_0 (mA cm^{-2})
WP-Mesop	0.5 M H_2SO_4	33	104	175	58	0.137
WP-Mesop-A		69	134	213	67	0.093
WP-Nano		111	187	275	76	0.024
WP-Bulk		172	257	370	95	0.018
WP-Mesop	1 M KOH	70	149	229	66	0.052
WP-Nano		175	257	376	84	0.007

states with BEs at 134.4 and 133.5 eV can also be found in surface P species. A slight surface oxidation would result in the distorted lattice fringes, which introduces more defects to the crystals (Figure S10).

To examine the electrocatalytic HER activity, the as-prepared powders were loaded onto a GC (3 mm) electrode with a loading of 2 mg cm^{-2}. For comparison, bare GC, commercial Pt/C (20%, Johnson Matthey), WP-Mesop-A, WP-Nano, WP-Nano-2, WP-Nano-4, and WP-Bulk were also tested under the same conditions. Figure 3a shows the

polarization curves in 0.5 M H_2SO_4 aqueous electrolyte. The commercial Pt/C catalyst shows the best HER activity with a near zero-onset overpotential, while bare GC exhibits negligible activity toward HER. The performance of each catalyst is summarized in Table 1. The onset potential of WP-Mesop is as low as 33 mV in 0.5 M H_2SO_4 solution. In comparison, the onset potentials increase to 69, 111, 97, 86, and 172 mV for WP-Mesop-A, WP-Nano, WP-Nano-2, WP-Nano-4, and WP-Bulk, respectively. Moreover, WP-Mesop yielded the lowest overpotential (η_{100}) of 175 mV at 100 mA
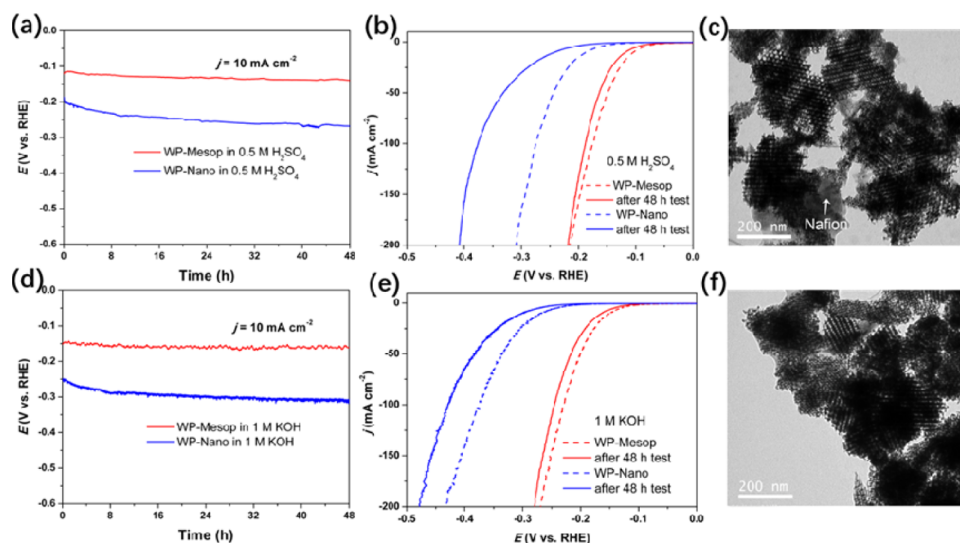
Figure 4. (a) Chronopotentiometry curves of WP-Mesop and WP-Nano under j = 10 mA cm^{-2} in 0.5 M H$_2$SO$_4$ solution. (b) LSV curves of WP-Mesop and WP-Nano before and after 48 h test in 0.5 M H$_2$SO$_4$ solution. (c) TEM image of WP-Mesop after 48 h test in 0.5 M H$_2$SO$_4$ solution. (d−f) Corresponding chronopotentiometry curves, LSV curves, and TEM image in 1 M KOH.

cm^{-2} among all samples. It is 38, 100, 85, 95, and 195 mV lower than those of WP-Mesop-A, WP-Nano, WP-Nano-2, WP-Nano-4, and WP-Bulk, respectively, as shown in Figure 3a.

The overpotential (η_{10}) for each sample to deliver a current density of 10 mA cm^{-2} is also compared. The η_{10} of WP-Mesop, WP-Mesop-A, WP-Nano, WP-Nano-2, WP-Nano-4, and WP-Bulk are 104, 134, 187, 175, 165, and 257 mV, respectively. Therefore, in the aspect of overpotential, WP-Mesop has great potential to be used as a HER catalyst, especially in the range of large current density (Figure 3b, Table S3).

The turnover frequencies (TOFs) were calculated by using the values of BET-specific surface areas.[48] Assuming that both W and P on the surface are active sites for WP-Mesop, while only W atoms are active sites for WP-Mesop-A and WP-Nano, as we discuss below. The calculated TOFs are 0.41, 0.39, and 0.15 s^{-1} for WP-Mesop, WP-Mesop-A, and WP-Nano at η_{200}, respectively. The larger TOF demonstrates the better catalytic activity of WP-Mesop.

Figure 3c shows the corresponding Tafel slopes of each electrocatalyst acquired from the linear section of LSV curves of HER. The Tafel slope of 31 mV/dec for Pt/C is consistent with the previous studies.[49,50] Here, the WP-Nano is prepared as a control sample because the small quantity of the W phase in WP-Nano has a small influence on HER activity, as shown in Figure 3a. The Tafel slope of WP-Mesop is 58 mV/dec in acid, which is much lower than that for WP-Nano (76 mV/dec) and WP-Bulk (95 mV/dec). The relatively low Tafel slope for WP-Mesop implies that HER proceeds via a Volmer−Heyrovsky mechanism, and electrochemical recombination with an additional proton is the rate-limiting step.[51] The lower Tafel slope observed in acid solution reveals faster charge-transfer kinetic for the WP-Mesop catalyst.

By extrapolating the linear part of the Tafel plots to an overpotential of 0 V, the intercept on the X-axis of the plot is the exchange current density j_0, as shown in Table 1. The j_0 value represents an intrinsic property of the catalyst materials, and a larger j_0 represents a faster electrochemical reaction rate of the electrodes at equilibrium.[52] The j_0 value of WP-Mesop is calculated to be 0.137 mA cm^{-2} in 0.5 M H$_2$SO$_4$, which is

higher than that of WP-Mesop-A (0.093 mA cm^{-2}), WP-Nano (0.024 mA cm^{-2}), and WP-Bulk (0.018 mA cm^{-2}). As compared with WP-Nano, the increase in j_0 is ∼6 times for WP-Mesop and ∼4 times for WP-Mesop-A, while the increase in BET-specific surface area is the same (∼2 times) for both. This indicates that both the mesoporosity and defect effects enhance HER activity. In particular, the mesoporosity contributes a bit more than the W vacancies do.

The electrochemical surface areas (ECSA) of WP-Mesop and WP-Nano were estimated from the cyclic voltammetry (CV) curves in 0.5 M H$_2$SO$_4$ to determine the real active areas. As shown in Figures 3d and S12, the electrochemical double-layer capacitance (C_{dl}) is normally used to estimate the ECSA. The calculated C_{dl} values of WP-Mesop and WP-Nano are 20 and 4 mF cm^{-2}, respectively. The larger ECSA of WP-Mesop, caused by the unique mesoporous structure and the W vacancies, can provide more active sites and facilitates gas diffusion, thus enhancing catalytic activity. Moreover, Figure S13 shows the replotted polarization curves of WP-Mesop and WP-Nano with current density normalized by ECSA. The WP-Mesop still exhibits better activity than WP-Nano, indicating superior intrinsic activity of the WP-Mesop.

EIS was conducted to investigate the HER kinetics of WP-Mesop and WP-Nano catalysts, as shown in Figure 3e. The Nyquist plots were fitted to the equivalent circuit, as shown in the inset of Figure 3e. The R_S component of the equivalent circuit represents the series resistance associated with the electrolyte and a series of contact resistances. The entire complex plane plots showed two semicircles. The smaller one in the high-frequency domain (inset of Figure 3e) could be attributed to the resistance of proton exchange membrane (R_{int}); and the larger one at a lower frequency can be attributed to the charge-transfer resistance (R_{ct}) of the HER.[49,53] The R_{ct} values of the two catalysts differ greatly. The WP-Mesop displays much smaller resistance (131 Ω) than the WP-Nano (540 Ω). This suggests faster HER kinetics for the WP-Mesop catalyst, which is consistent with the Tafel slope.

Furthermore, we also tested HER performance of WP-Mesop, WP-Nano, and 20% Pt/C in 1 M KOH solution. The η_{10} and η_{100} of WP-Mesop (149 and 229 mV) are much lower

than those of WP-Nano (257 and 376 mV), exhibiting the same trend as in acid solution. The Tafel slope of WP-Mesop is 66 mV/dec, lower than 84 mV/dec of WP-Nano, as listed in Table 1. The small Tafel slope of WP-Mesop in alkaline media indicates the same fast Volmer−Heyrovsky HER pathway as in acid media. These results demonstrate that the WP-Mesop possesses superior HER activity in both acid and alkaline solutions. Moreover, the overpotential is lower than the reported defect-rich WP and is comparable to the recently reported state-of-art MoS_2 quantum dots (acid: $\eta_{10} \approx 92$ mV, $\eta_{100} > 300$ mV), N-doped WC (acid: $\eta_{10} \approx 89$ mV, $\eta_{100} > 160$ mV), and P−Co_3O_4 (alkaline: $\eta_{10} \approx 120$ mV) non-noble metal catalysts.[7,11,35,54]

Durability is another important factor in evaluating electrocatalyst performance. A constant current density of 10 mA cm^{-2} was applied to investigate the long-term stability both in 0.5 M H_2SO_4 and 1 M KOH solutions. As shown in Figure 4a,b, WP-Mesop shows stability superior to WP-Nano after 48 h. The WP-Mesop catalyst constantly produces H_2 under the constant current density for 48 h with only 18 and 9 mV increase in the applied bias in acid and in alkaline media, respectively. However, the increments in overpotential are 62 mV (acid) and 80 mV (alkaline) for WP-Nano under the same conditions.

Figure 4c,d shows the polarization curves of each catalyst before and after a 48 h test. The polarization curves of the spent WP-Mesop are almost the same as the fresh catalyst with only a small positive shift (∼14 mV) of η_{10} in both acid and alkaline media after HER for 48 h. In comparison, WP-Nano exhibits inferior stability. Its surface may gradually deactivate by corrosion during the process. After 48 h, the WP-Mesop catalyst was scraped off the GC electrode and washed. Figure 4e,f shows TEM images of WP-Mesop after 48 h test in 0.5 M H_2SO_4 and 1 M KOH solutions. The TEM images show that the mesoporous structure is maintained after 48 h in both acid and alkaline media, as well as its crystallinity (Figure S14), indicating good corrosion resistance and structure stability of the mesoporous catalyst. In general, the dissolution of transitional metals is thermodynamically less favorable for phosphides.[55] The abundant W vacancies mean higher P content at the solid−liquid interface, which can prevent corrosion.

DFT calculations suggest that the W vacancies have great impact on enhancing HER activity (details in the Supporting Information). The Gibbs free energy of the adsorbed state H* (ΔG_{H*}) has been used to describe the HER activity of electrocatalysts. The optimal value of ΔG_{H*} for an electrocatalyst should be close to zero.[56−58] The calculated free energies for (101) surfaces of pristine WP and defective WP are shown in Figure 5. The ΔG_{H*} value of the most active sites for pristine WP are −0.087 eV for W site and 0.899 eV for P site. However, for defective WP (WP-Mesop), the most active sites possess especially small ΔG_{H*} of −0.034 eV (W site) and 0.051 eV (P site), closer to the ideal value ($\Delta G_{H*} = 0$ eV). The near-zero ΔG_{H*} for WP-Mesop suggests that H atoms react easily on defect surfaces, facilitating HER. Moreover, our calculations indicate that hydrogen atoms are more inclined to be adsorbed on W ($|\Delta G_{H*}| < 0.182$ eV) sites rather than P ($\Delta G_{H*} = 0.899$ eV) for pristine WP (Table S4). However, in addition to the lower activation barrier of W sites, the P sites may become new active sites ($|\Delta G_{H*}| < 0.145$ eV) when there is a W vacancy nearby. These more active sites would further
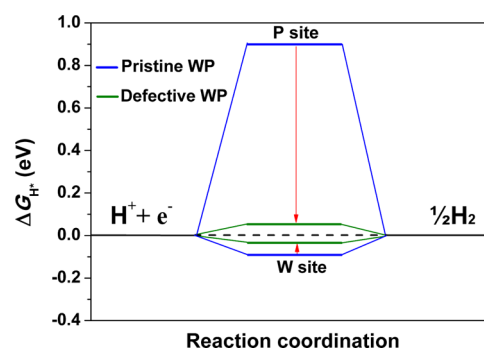
Figure 5. Free-energy diagrams for most active sites on the (101) surface of pristine and defective WP.

enhance the HER activity, which is consistent with the experimental results.

4. CONCLUSIONS

In summary, we propose a new strategy to in situ synthesize cation vacancies using a vacuum-assisted nanocasting method. The results have demonstrated that the W vacancies in WP can be introduced by preventing P loss during the reduction process in the limited mesopores. The mesoporous structure of the catalyst with higher specific surface area provides more active sites for HER. The W vacancies further enhance the intrinsic activity and corrosion resistance. The combination of the unique mesoporous structure and abundant W vacancies endows WP-Mesop with excellent activity and enhanced stability for HER in both acid and alkaline media. Our present study not only offers an inexpensive catalyst with high activity for HER but also provides a facile route to introduce abundant cation vacancies in TMPs by the confinement effect of mesopores.

■ ASSOCIATED CONTENT

Supporting Information

The Supporting Information is available free of charge at https://pubs.acs.org/doi/10.1021/acsami.9b22761.

> TEM image, SAXS pattern, and nitrogen adsorption−desorption isotherm curve of KIT-6 template; additional TEM, HR-STEM images, and nitrogen adsorption−desorption isotherm curves for WP-Mesop; TEM images for WP-Mesop-A, WP-Nano, WP-Nano-2, WP-Nano-4, and WP-Bulk; XRD and TEM images for WP-Mesop (P/W = 2); CV results for RHE calibration; CVs for double-layer capacitance; XRD patterns of WP-Mesop after stability test; EDX and XPS results of element content, a summarized HER performance; and additional DFT calculation results (PDF)

■ AUTHOR INFORMATION

Corresponding Authors

Jing Liu − School of Materials Science and Engineering, Shanghai Jiao Tong University, Shanghai 200240, China; orcid.org/0000-0002-9377-1626; Email: liujing2014@sjtu.edu.cn

Peng Zhang − School of Materials Science and Engineering, Shanghai Jiao Tong University, Shanghai 200240, China; orcid.org/0000-0001-6834-4190; Email: pengzhang2010@sjtu.edu.cn

Authors

Feng Li − *School of Materials Science and Engineering, Shanghai Jiao Tong University, Shanghai 200240, China*

Chengru Wang − *School of Materials Science and Engineering, Shanghai Jiao Tong University, Shanghai 200240, China;* orcid.org/0000-0002-9033-3030

Xiaocang Han − *School of Materials Science and Engineering, Shanghai Jiao Tong University, Shanghai 200240, China*

Xiaoqian Feng − *School of Materials Science and Engineering, Shanghai Jiao Tong University, Shanghai 200240, China*

Yuqi Qu − *School of Materials Science and Engineering, Shanghai Jiao Tong University, Shanghai 200240, China*

Wenlong Chen − *School of Materials Science and Engineering, Shanghai Jiao Tong University, Shanghai 200240, China*

Liping Zhao − *School of Materials Science and Engineering, Shanghai Jiao Tong University, Shanghai 200240, China*

Xuefeng Song − *School of Materials Science and Engineering, Shanghai Jiao Tong University, Shanghai 200240, China;* orcid.org/0000-0003-4251-3720

Hong Zhu − *School of Materials Science and Engineering, Shanghai Jiao Tong University, Shanghai 200240, China;* orcid.org/0000-0001-7919-5661

Han Chen − *School of Materials Science and Engineering, Shanghai Jiao Tong University, Shanghai 200240, China*

Min Zhao − *State Key Laboratory of Ocean Engineering, School of Naval Architecture, Shanghai Jiao Tong University, Shanghai 200240, China*

Zhao Deng − *Soochow Institute for Energy and Materials Innovations, College of Energy, Soochow University, Suzhou 215006, China;* orcid.org/0000-0002-0008-5759

Jianbo Wu − *School of Materials Science and Engineering and State Key Laboratory of Metal Matrix Composites and Center of Hydrogen Science, Shanghai Jiao Tong University, Shanghai 200240, China;* orcid.org/0000-0002-3574-5585

Lian Gao − *School of Materials Science and Engineering, Shanghai Jiao Tong University, Shanghai 200240, China*

Complete contact information is available at:
https://pubs.acs.org/10.1021/acsami.9b22761

Notes
The authors declare no competing financial interest.

REFERENCES

(1) Zheng, Y.; Jiao, Y.; Vasileff, A.; Qiao, S.-Z. The Hydrogen Evolution Reaction in Alkaline Solution: From Theory, Single Crystal Models, to Practical Electrocatalysts. *Angew. Chem., Int. Ed.* **2018**, *57*, 7568−7579.

(2) Wang, Y.; Yan, D.; El Hankari, S.; Zou, Y.; Wang, S. Recent Progress on Layered Double Hydroxides and Their Derivatives for Electrocatalytic Water Splitting. *Adv. Sci.* **2018**, *5*, 1800064.

(3) Yu, J.; Li, W.-J.; Zhang, H.; Zhou, F.; Li, R.; Xu, C.-Y.; Zhou, L.; Zhong, H.; Wang, J. Metallic FePSe₃ Nanoparticles Anchored on N-doped Carbon Framework for All-pH Hydrogen Evolution Reaction. *Nano Energy* **2019**, *57*, 222−229.

(4) Feng, J.-X.; Tong, S.-Y.; Tong, Y.-X.; Li, G.-R. Pt-like Hydrogen Evolution Electrocatalysis on PANI/CoP Hybrid Nanowires by Weakening the Shackles of Hydrogen Ions on the Surfaces of Catalysts. *J. Am. Chem. Soc.* **2018**, *140*, 5118−5126.

(5) Xu, Y.-T.; Xiao, X.; Ye, Z.-M.; Zhao, S.; Shen, R.; He, C.-T.; Zhang, J.-P.; Li, Y.; Chen, X.-M. Cage-Confinement Pyrolysis Route to Ultrasmall Tungsten Carbide Nanoparticles for Efficient Electrocatalytic Hydrogen Evolution. *J. Am. Chem. Soc.* **2017**, *139*, 5285−5288.

(6) Ren, B.; Li, D.; Jin, Q.; Cui, H.; Wang, C. Novel Porous Tungsten Carbide Hybrid Nanowires on Carbon Cloth for High-performance Hydrogen Evolution. *J. Mater. Chem. A* **2017**, *5*, 13196−13203.

(7) Han, N.; Yang, K. R.; Lu, Z.; Li, Y.; Xu, W.; Gao, T.; Cai, Z.; Zhang, Y.; Batista, V. S.; Liu, W.; Sun, X. Nitrogen-doped Tungsten Carbide Nanoarray as an Efficient Bifunctional Electrocatalyst for Water Splitting in Acid. *Nat. Commun.* **2018**, *9*, 924.

(8) Yu, H.; Yang, X.; Xiao, X.; Chen, M.; Zhang, Q.; Huang, L.; Wu, J.; Li, T.; Chen, S.; Song, L.; Gu, L.; Xia, B. Y.; Feng, G.; Li, J.; Zhou, J. Atmospheric-Pressure Synthesis of 2D Nitrogen-Rich Tungsten Nitride. *Adv. Mater.* **2018**, *30*, 1805655.

(9) Jin, H.; Liu, X.; Jiao, Y.; Vasileff, A.; Zheng, Y.; Qiao, S.-Z. Constructing Tunable Dual Active Sites on Two-Dimensional C₃N₄@MoN Hybrid for Electrocatalytic Hydrogen Evolution. *Nano Energy* **2018**, *53*, 690−697.

(10) Bentley, C. L.; Andronescu, C.; Smialkowski, M.; Kang, M.; Tarnev, T.; Marler, B.; Unwin, P. R.; Apfel, U.-P.; Schuhmann, W. Local Surface Structure and Composition Control the Hydrogen Evolution Reaction on Iron Nickel Sulfides. *Angew. Chem., Int. Ed.* **2018**, *57*, 4093−4097.

(11) Chen, W.; Gu, J.; Liu, Q.; Luo, R.; Yao, L.; Sun, B.; Zhang, W.; Su, H.; Chen, B.; Liu, P.; Zhang, D. Quantum Dots of 1T Phase Transitional Metal Dichalcogenides Generated via Electrochemical Li Intercalation. *ACS Nano* **2018**, *12*, 308−316.

(12) Zhou, Y.; Song, E.; Zhou, J.; Lin, J.; Ma, R.; Wang, Y.; Qiu, W.; Shen, R.; Suenaga, K.; Liu, Q.; Wang, J.; Liu, Z.; Liu, J. Auto-optimizing Hydrogen Evolution Catalytic Activity of ReS₂ through Intrinsic Charge Engineering. *ACS Nano* **2018**, *12*, 4486−4493.

(13) Wu, Y.; Li, F.; Chen, W.; Xiang, Q.; Ma, Y.; Zhu, H.; Tao, P.; Song, C.; Shang, W.; Deng, T.; Wu, J. Coupling Interface Constructions of MoS₂/Fe₅Ni₄S₈ Heterostructures for Efficient Electrochemical Water Splitting. *Adv. Mater.* **2018**, *30*, 1803151.

(14) Chen, Y.; Zhang, J.; Guo, P.; Liu, H.; Wang, Z.; Liu, M.; Zhang, T.; Wang, S.; Zhou, Y.; Lu, X.; Zhang, J. Coupled Heterostructure of Mo-Fe Selenide Nanosheets Supported on Carbon Paper as an Integrated Electrocatalyst for Efficient Hydrogen Evolution. *ACS Appl. Mater. Interfaces* **2018**, *10*, 27787−27794.

(15) Zhou, Q.; Shen, Z.; Zhu, C.; Li, J.; Ding, Z.; Wang, P.; Pan, F.; Zhang, Z.; Ma, H.; Wang, S.; Zhang, H. Nitrogen-Doped CoP Electrocatalysts for Coupled Hydrogen Evolution and Sulfur Generation with Low Energy Consumption. *Adv. Mater.* **2018**, *30*, 1800140.

(16) Wang, X.-D.; Xu, Y.-F.; Rao, H.-S.; Xu, W.-J.; Chen, H.-Y.; Zhang, W.-X.; Kuang, D.-B.; Su, C.-Y. Novel Porous Molybdenum Tungsten Phosphide Hybrid Nanosheets on Carbon Cloth for Efficient Hydrogen Evolution. *Energy Environ. Sci.* **2016**, *9*, 1468−1475.

(17) Yang, Y.; Luo, M.; Xing, Y.; Wang, S.; Zhang, W.; Lv, F.; Li, Y.; Zhang, Y.; Wang, W.; Guo, S. A Universal Strategy for Intimately Coupled Carbon Nanosheets/MoM Nanocrystals (M = P, S, C, and O) Hierarchical Hollow Nanospheres for Hydrogen Evolution Catalysis and Sodium-Ion Storage. *Adv. Mater.* **2018**, *30*, 1706085.

(18) Pu, Z.; Ya, X.; Amiinu, I. S.; Tu, Z.; Liu, X.; Li, W.; Mu, S. Ultrasmall Tungsten Phosphide Nanoparticles Embedded in Nitro-

gen-Doped Carbon as A Highly Active and Stable Hydrogen-Evolution Electrocatalyst. *J. Mater. Chem. A* **2016**, *4*, 15327−15332.

(19) Du, H.; Kong, R.-M.; Guo, X.; Qu, F.; Li, J. Recent Progress in Transition Metal Phosphides with Enhanced Electrocatalysis for Hydrogen Evolution. *Nanoscale* **2018**, *10*, 21617−21624.

(20) Wang, Q.; Liu, Z.; Zhao, H.; Huang, H.; Jiao, H.; Du, Y. MOF-derived Porous Ni_2P Nanosheets as Novel Bifunctional Electrocatalysts for the Hydrogen and Oxygen Evolution Reactions. *J. Mater. Chem. A* **2018**, *6*, 18720−18727.

(21) Guan, C.; Xiao, W.; Wu, H.; Liu, X.; Zang, W.; Zhang, H.; Ding, J.; Feng, Y. P.; Pennycook, S. J.; Wang, J. Hollow Mo-doped CoP Nanoarrays for Efficient Overall Water Splitting. *Nano Energy* **2018**, *48*, 73−80.

(22) Wu, T.; Pi, M.; Zhang, D.; Chen, S. Three-dimensional Porous Structural MoP_2 Nanoparticles as a Novel and Superior Catalyst for Electrochemical Hydrogen Evolution. *J. Power Sources* **2016**, *328*, 551−557.

(23) Sumboja, A.; An, T.; Goh, H. Y.; Lübke, M.; Howard, D. P.; Xu, Y.; Handoko, A. D.; Zong, Y.; Liu, Z. One-Step Facile Synthesis of Cobalt Phosphides for Hydrogen Evolution Reaction Catalysts in Acidic and Alkaline Medium. *ACS Appl. Mater. Interfaces* **2018**, *10*, 15673−15680.

(24) Liu, T.; Li, P.; Yao, N.; Cheng, G.; Chen, S.; Luo, W.; Yin, Y. CoP-Doped MOF-Based Electrocatalyst for pH-Universal Hydrogen Evolution Reaction. *Angew. Chem., Int. Ed.* **2019**, *58*, 4679−4684.

(25) Wang, J.; Chang, K.; Sun, Z.; Lee, J. H.; Tackett, B. M.; Zhang, C.; Chen, J. G.; Liu, C.-J. A Combined Experimental and Theoretical Study of the Accelerated Hydrogen Evolution Kinetics over Wide pH Range on Porous Transition Metal Doped Tungsten Phosphide Electrocatalysts. *Appl. Catal., B* **2019**, *251*, 162−167.

(26) Wu, L.; Pu, Z.; Tu, Z.; Amiinu, I. S.; Liu, S.; Wang, P.; Mu, S. Integrated Design and Construction of WP/W Nanorod Array Electrodes Toward Efficient Hydrogen Evolution Reaction. *Chem. Eng. J.* **2017**, *327*, 705−712.

(27) Pu, Z.; Liu, Q.; Asiri, A. M.; Sun, X. Tungsten Phosphide Nanorod Arrays Directly Grown on Carbon Cloth: A Highly Efficient and Stable Hydrogen Evolution Cathode at All pH Values. *ACS Appl. Mater. Interfaces* **2014**, *6*, 21874−21879.

(28) Yan, X.; Jia, Y.; Yao, X. Defects on Carbons for Electrocatalytic Oxygen Reduction. *Chem. Soc. Rev.* **2018**, *47*, 7628−7658.

(29) Yan, D.; Li, Y.; Huo, J.; Chen, R.; Dai, L.; Wang, S. Defect Chemistry of Nonprecious-Metal Electrocatalysts for Oxygen Reactions. *Adv. Mater.* **2017**, *29*, 1606459.

(30) Dou, S.; Tao, L.; Wang, R.; El Hankari, S.; Chen, R.; Wang, S. Plasma-Assisted Synthesis and Surface Modification of Electrode Materials for Renewable Energy. *Adv. Mater.* **2018**, *30*, 1705850.

(31) Dong, Y.; Zhang, S.; Du, X.; Hong, S.; Zhao, S.; Chen, Y.; Chen, X.; Song, H. Boosting the Electrical Double-Layer Capacitance of Graphene by Self-Doped Defects through Ball-Milling. *Adv. Funct. Mater.* **2019**, *29*, 1901127.

(32) Wang, X.; Zhuang, L.; Jia, Y.; Liu, H.; Yan, X.; Zhang, L.; Yang, D.; Zhu, Z.; Yao, X. Plasma-Triggered Synergy of Exfoliation, Phase Transformation, and Surface Engineering in Cobalt Diselenide for Enhanced Water Oxidation. *Angew. Chem., Int. Ed.* **2018**, *57*, 16421−16425.

(33) Ye, G.; Gong, Y.; Lin, J.; Li, B.; He, Y.; Pantelides, S. T.; Zhou, W.; Vajtai, R.; Ajayan, P. M. Defects Engineered Monolayer MoS2 for Improved Hydrogen Evolution Reaction. *Nano Lett.* **2016**, *16*, 1097−1103.

(34) Cui, X.; Pan, Z.; Zhang, L.; Peng, H.; Zheng, G. Selective Etching of Nitrogen-doped Carbon by Steam for Enhanced Electrochemical CO_2 Reduction. *Adv. Energy Mater.* **2017**, *7*, 1701456.

(35) Xiao, Z.; Wang, Y.; Huang, Y.-C.; Wei, Z.; Dong, C.-L.; Ma, J.; Shen, S.; Li, Y.; Wang, S. Filling the Oxygen Vacancies in Co_3O_4 with Phosphorus: An Ultra-efficient Electrocatalyst for Overall Water Splitting. *Energy Environ. Sci.* **2017**, *10*, 2563−2569.

(36) Kwong, W. L.; Gracia-Espino, E.; Lee, C. C.; Sandström, R.; Wågberg, T.; Messinger, J. Cationic Vacancy Defects in Iron

Phosphide: A Promising Route toward Efficient and Stable Hydrogen Evolution by Electrochemical Water Splitting. *ChemSusChem* **2017**, *10*, 4544−4551.

(37) Yu, P.; Wang, F.; Shifa, T. A.; Zhan, X.; Lou, X.; Xia, F.; He, J. Earth Abundant Materials beyond Transition Metal Dichalcogenides: A Focus on Electrocatalyzing Hydrogen Evolution Reaction. *Nano Energy* **2019**, *58*, 244−276.

(38) Sun, H.; Xu, X.; Yan, Z.; Chen, X.; Cheng, F.; Weiss, P. S.; Chen, J. Porous Multishelled Ni_2P Hollow Microspheres as an Active Electrocatalyst for Hydrogen and Oxygen Evolution. *Chem. Mater.* **2017**, *29*, 8539−8547.

(39) Hu, E.; Feng, Y.; Nai, J.; Zhao, D.; Hu, Y.; Lou, X. W. Construction of Hierarchical Ni−Co−P Hollow Nanobricks with Oriented Nanosheets for Efficient Overall Water Splitting. *Energy Environ. Sci.* **2018**, *11*, 872−880.

(40) Kleitz, F.; Hei Choi, S.; Ryoo, R. Cubic Ia3d Large Mesoporous Silica: Synthesis and Replication to Platinum Nanowires, Carbon Nanorods and Carbon Nanotubes. *Chem. Commun.* **2003**, 2136−2137.

(41) Grimme, S. Semiempirical GGA-type density functional constructed with a long-range dispersion correction. *J. Comput. Chem.* **2006**, *27*, 1787−1799.

(42) Kresse, G. Efficient Iterative Schemes for ab Initio Total-energy Calculations Using a Plane-wave Basis Set. *Phys. Rev. B: Condens. Matter Mater. Phys.* **1996**, *54*, 11169−11186.

(43) Blöchl, P. E. Projector Augmented-wave Method. *Phys. Rev. B: Condens. Matter Mater. Phys.* **1994**, *50*, 17953−17979.

(44) Nørskov, J. K.; Bligaard, T.; Logadottir, A.; Kitchin, J. R.; Chen, J. G.; Pandelov, S.; Stimming, U. Trends in the Exchange Current for Hydrogen Evolution. *J. Electrochem. Soc.* **2005**, *152*, J23−J26.

(45) Koketsu, T.; Ma, J.; Morgan, B. J.; Body, M.; Legein, C.; Dachraoui, W.; Giannini, M.; Demortière, A.; Salanne, M.; Dardoize, F.; Groult, H.; Borkiewicz, O. J.; Chapman, K. W.; Strasser, P.; Dambournet, D. Reversible Magnesium and Aluminium Ions Insertion in Cation-deficient Anatase TiO_2. *Nat. Mater.* **2017**, *16*, 1142−1148.

(46) Fang, H.; Roldan, A.; Tian, C.; Zheng, Y.; Duan, X.; Chen, K.; Ye, L.; Leoni, S.; Yuan, Y. Structural tuning and catalysis of tungsten carbides for the regioselectivecleavage of CAO bonds. *J. Catal.* **2019**, *369*, 283−295.

(47) Zhang, X.; Wang, J.; Guo, T.; Liu, T.; Wu, Z.; Cavallo, L.; Cao, Z.; Wang, D. Structure and Phase Regulation in Mo_xC (α-MoC_{1-x}/β-Mo_2C) to Enhance Hydrogen Evolution. *Appl. Catal., B* **2019**, *247*, 78−85.

(48) Popczun, E. J.; Mckone, J. R.; Read, C. G.; Biacchi, A. J.; Wiltrout, A. M.; Lewis, N. S.; Schaak, R. E. Nanostructured Nickel Phosphide as an Electrocatalyst for the Hydrogen Evolution Reaction. *J. Am. Chem. Soc.* **2013**, *135*, 9267−9270.

(49) Kuang, P.; Tong, T.; Fan, K.; Yu, J. In Situ Fabrication of Ni−Mo Bimetal Sulfide Hybrid as an Efficient Electrocatalyst for Hydrogen Evolution over a Wide pH Range. *ACS Catal.* **2017**, *7*, 6179−6187.

(50) Cheng, R.; He, H.; Pu, Z.; Amiinu, I. S.; Chen, L.; Wang, Z.; Li, G.; Mu, S. Shrunken Hollow Mo-N/Mo-C Nanosphere Structure for Efficient Hydrogen Evolution in a Broad pH Range. *Electrochim. Acta* **2019**, *298*, 799−805.

(51) Xiao, P.; Sk, M. A.; Thia, L.; Ge, X.; Lim, R. J.; Wang, J.-Y.; Lim, K. H.; Wang, X. Molybdenum Phosphide as an Efficient Electrocatalyst for the Hydrogen Evolution Reaction. *Energy Environ. Sci.* **2014**, *7*, 2624−2629.

(52) Shi, Y.; Zhang, B. Recent Advances in Transition Metal Phosphide Nanomaterials: Synthesis and Applications in Hydrogen Evolution Reaction. *Chem. Soc. Rev.* **2016**, *45*, 1529−1541.

(53) Chen, Z.; Yu, A.; Ahmed, R.; Wang, H.; Li, H.; Chen, Z. Manganese Dioxide Nanotube and Nitrogen-doped Carbon Nanotube Based Composite Bifunctional Catalyst for Rechargeable Zinc-air Battery. *Electrochim. Acta* **2012**, *69*, 295−300.

(54) Zhang, X.; Guo, T.; Liu, T.; Lv, K.; Wu, Z.; Wang, D. Tungsten Phosphide (WP) Nanoparticles with Tunable Crystallinity, W

Vacancies, and Electronic Structures for Hydrogen Production. *Electrochim. Acta* **2019**, *323*, 134798.

(55) Kucernak, A. R. J.; Naranammalpuram Sundaram, V. N. Nickel Phosphide: The Effect of Phosphorus Content on Hydrogen Evolution Activity and Corrosion Resistance in Acidic Medium. *J. Mater. Chem. A* **2014**, *2*, 17435−17445.

(56) Ma, Y.; Yu, G.; Wang, T.; Zhang, C.; Huang, X.; Chen, W. Highly Efficient Catalytic Activity for the Hydrogen Evolution Reaction on Pristine and Monovacancy Defected WP Systems: A First-Principles Investigation. *Phys. Chem. Chem. Phys.* **2018**, *20*, 13757−13764.

(57) Liu, P.; Rodriguez, J. A. Catalysts for Hydrogen Evolution from the [NiFe] Hydrogenase to the Ni_2P (001) Surface: The Importance of Ensemble Effect. *J. Am. Chem. Soc.* **2005**, *127*, 14871−14878.

(58) Li, H.; Wen, P.; Itanze, D. S.; Kim, M. W.; Adhikari, S.; Lu, C.; Jiang, L.; Qiu, Y.; Geyer, S. M. Phosphorus-Rich Colloidal Cobalt Diphosphide (CoP_2) Nanocrystals for Electrochemical and Photo-electrochemical Hydrogen Evolution. *Adv. Mater.* **2019**, *31*, 1900813.